

Preliminary geometrical and microstructural characterization of WC-reinforced NiCrBSi matrix composites fabricated by plasma transferred arc additive manufacturing through Taguchi-based experimentation

J.G. Mercado Rojas · M. Ghasri-Khouzani · T. Wolfe · B.A. Fleck · H. Henein · Ahmed Jawad Qureshi

Received: date / Accepted: date

Abstract Metal matrix composites enhance the wear and corrosion properties of components in heavy-duty industries. This work reports the preliminary effects of process parameters such as current, linear speed, powder flow rate, nozzle angle, and powder, shield and center gases at the macro-scale and micro-scale of single-track multiple-layers depositions. The use of plasma transferred arc as an additive manufacturing system acquiesce to generate enough energy for a fast solidification rate of the matrix without compromising the carbide in the composite. The results show that the bead height is mainly affected by the powder flow rate, the powder gas, and the travel speed at the macro-scale. The bead width has a close relationship with powder flow rate, powder gas, and current, the latter contributing to the formation of a slumping phenomenon due to heat accumulation. The volumetric deposition is affected by similar parameters to the bead height. At the micro-scale, the process parameters did not show significant carbide changes but validate its homogeneous distribution. The electron microscope observation exhibited the composite's high quality due to the fast solidification of the process. Results demonstrate that the porosity is mainly affected by the powder flow rate. By understanding the preliminary contribution of process parameters, this manufacturing process can print near net-shaped parts minimizing the post-processing of metal additive manufacturing components. There-

fore, this work contributes to implementing a preliminary experimental methodology to understand the deposition process of WC-reinforced composites in plasma transferred arc additive manufacturing.

Keywords Additive manufacturing · Metal matrix composite · NiCrBSi · Taguchi design of experiments · Plasma transferred arc · PTA-AM

1 Introduction

The development of new technology in Additive Manufacturing (AM) has promoted the formation of new applications in various industrial sectors. In the metal AM scope, heavy-duty industries demand for 3D printed components capable of withstanding the severe conditions associated with the working conditions such as abrasion, impact, and erosion. Plasma Transferred Arc (PTA) is commonly used to deposit thick overlays of high wear and corrosion-resistant alloys with high deposition speeds [1]. Mercado Rojas et al. [2] confirmed that this technology can be adapted as a metal additive manufacturing process named PTA-AM for printing Metal Matrix Composites (MMC) with characteristics comparable to typical composite coatings for the heavy industry [3]. Moreover, this technology can be classified as a Direct Energy Deposition (DED) AM system where a concentrated energy source and a stream of raw material intersect at a focal point giving rise to melt pool formation [4] (Fig. 1).

DED-AM are non-equilibrium processes with fast cooling rates, a diverse set of processing parameters coupled with complex transportation phenomena bears to a difficulty in understanding the particular effects of process parameters [5]. Generally, the determination of

J.G. Mercado Rojas
Department of Mechanical Engineering, University of Alberta, Edmonton, AB, T6G 2G8, Canada
E-mail: mercador@ualberta.ca

Ahmed Jawad Qureshi
Department of Mechanical Engineering, University of Alberta, Edmonton, AB, T6G 2G8, Canada
E-mail: ajquresh@ualberta.ca

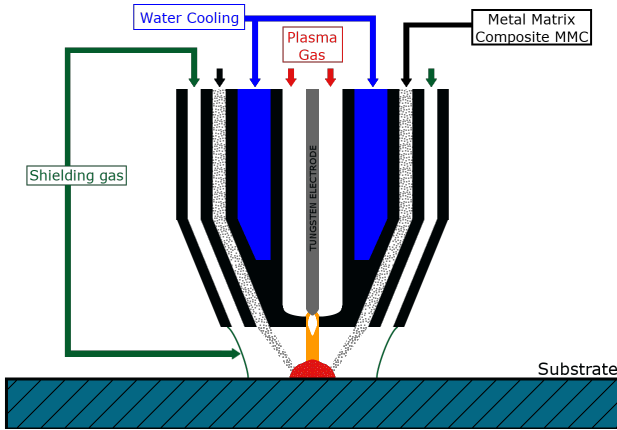


Fig. 1: Plasma Transferred Arc deposition.

process parameters in new AM systems consists of trial-and-error round-robin tests. Artaza et al. [6] designed and integrated a Wire and Arc Additive Manufacturing (WAAM) system to print Ti-6Al-4V components. The validation of the technique required a combination of 83 single depositions varying feed rate, current, and wire feed speed for a single material. Although these tests can determine the working conditions for the system, further knowledge is required to achieve near net-shaped components [7]. Understanding the role of these variables in metal AM deposition improves the printing quality of components. In PTA-AM, the combination of process parameters such as current, linear speed, powder flow rate, nozzle angle, and powder, shield and center gas flows leads to particular characteristics. The metal deposition rates and quality, different penetration levels into the substrate, losses of powder material, and specific bead height and width are characteristics dependant on process parameters achievable rapidly in a single pass [8].

The effects of process parameters can be determined through the Design of Experiments (DOE). This systematic layout of experimentation improves the time efficiency of one-factor-at-a-time experiments, avoids misleading conditions in the presence of interaction, and estimates the effect of parameters at different levels [9]. These type of experiments have been used to investigate the deposition rate in twin-wire submerged arc welding [10] and tungsten inert gas welding [11]. Similarly, DOEs have been used to link process parameters to bead characteristics in laser cladding [12, 13, 14] and plasma cladding [15]. Wilden et al. [16], and Parekh et al. [17] used the experiments for multiphysics simulation in PTA welding and laser cladding, respectively. Other researchers analyzed the effects of process parameters in the bead geometry through transient stud-

ies [18, 19].

In terms of metal AM for DED systems, process parameters research through DOEs focus on laser and WAAM systems. Table 1 provides insight into the input and output criterion for laser beam experiments. It is important to note that laser beam observations mainly centers on stainless steel. Standard process parameters are laser power, laser velocity, and powder feed rate. In the outcome measures, the bead geometry, such as width and height, are typically investigated.

Beuth and Klingbeil [20] described the use of a process map approach for the relationship between process parameters and critical deposition parameters such as melt pool size, residual stress, and grain size. In Fathi et al. [21], a theoretical model was linked to the numerical results from the evaluated experiments. A case study for building airfoils with three-, and four-way nozzles was conducted by Qi et al. [22] showed a central composite design to drive the experiments. Additionally, Angelastro et al. [23] described the comparisons between a mathematical model and the results of multi-layer claddings built with MMC composites. A finite element model in single-track single-layer beads was applied by Amine et al. [24] to compare the experimental results and to obtain temperature readings, microstructure analysis, and microhardness and grain size measurement. Saqib et al. [25] used experimental results to build a prediction model through ANOVA, lumped parameters, and artificial neural networks. Single- and multiple-layers depositions were employed to build contour plots correlating process parameters to thin wall structure height [26].

Table 2 presents similar information as Table 1, but for WAAM systems. Wire feed speed is a standard parameter along with the studies. In these cases, alloys' availability is limited to commercially wire forms. Prado-Cerqueira et al. [27] implemented a hybrid process to metal 3D printing and milling for surface finishing components. The results from more than 100 experiments related the process parameters to bead height and width. In Liberini et al. [28], the research focused on comparing microstructure and mechanical properties by varying the input parameters. Porosity in single-track multiple layers beads is measured and evaluated considering different manufacturing process parameters and material batches [29]. Furthermore, by building thin walls, Zhang et al. [30] created AM transverse and longitudinal tensile tests linking process parameters with ultimate tensile strength and grain maps.

Table 1: Literature review for process parameters in Laser beam systems.

Study	Process parameter	Outcome measures	Material
[20]	-Laser power -Laser velocity -Preheating temperatures -Part geometry	-Melt pool size -Grain size -Residual stress	304 stainless steel
[21]	-Laser power -Laser velocity	-Bead height -Bead width -Dilution	303L Stainless steel
[22]	-Laser power -Defocus distance -Powder feed rate -Travel speed -Height increment -Shield gas flow	-Wall thickness -Layer height	Inconel 718
[23]	-Laser speed -Hatching space X -Hatching space Z	-Bead width -Bead height -Deposition efficiency	30% Colmonoy 227-F 70% WC/Co/Cr
[24]	-Laser power -Traverse speed -Powder feed rate	-Hardness -Temperature and solidification ratio -Grain size -Temperature -Bead height	316L Stainless steel
[25]	-Laser power -Powder feed rate -Laser speed -Focal length -Contact tip distance	-Bead width -Bead height -Penetration -Positive area -Negative area	P420 Stainless Steel
[26]	-Pulse energy -Pulse duration -Transverse speed -Height increment	-Bead width -Bead height -Penetration -Deposited area	301L Stainless Steel

Although less popular, other types of energy sources were analyzed (Table 3). Travel speed, power-related parameters, and material deposition rate were standardized process parameters, while bead height and bead width were outcome measurements. In Wang et al. [8], voltage information controlled the arc length in μ -plasma, and their system built functionally graded components. Likewise, Jhavar et al. [31] correlated process parameters of multiple layer depositions to quality deposition and characteristics such as surface waviness, deposition efficiency, and microhardness. Moreover, Sawant and Jain [32] investigated the coefficient of friction, wear volume variation, lamellae width, and microhardness. In plasma wire deposition, Martina et al. [33] studied a cubic behaviour with three-factor third-order polynomial function to fit experiments and obtain a working envelope.

While previous work in Mercado Rojas et al. [2] has proven PTA-AM technology to be suitable, the research presented here aims to preliminary understand the influence of process parameters in the bead geometry and the microstructure of WC-reinforced compos-

ites through the use of PTA-AM. The next section describes the materials and methods for the experiments. This section details the analyzed process parameters, the Taguchi-based DOE model, and the acquisition of outcome measures.

2 Materials and methods

Figure 2 shows the PTA-AM system. It consists of a Kennametal StelliteTMSTARWELD 400A PTA system. It is designed for general-purpose, multi-faceted, hard face production though the spread of fully fused metal deposits. Typically, metal powder is carried from a powder feeder to the torch in an argon stream. The powder torrent transports the material into the plasma, here it is melted and fusion bonded to the workpiece. A direct current power source provides the energy for the transferred arc across a tungsten electrode. For the hard-facing PTA system be modified into an AM system, a 3-axis coordinated positioning device is positioned under the torch while the torch travel remains fixed. The PTA positioning device yields the flexibility to move on

Table 2: Literature review for process parameters in WAAM systems.

Study	Process parameter	Outcome measures	Material
[27]	-Welding speed -Current -Arc correction -Dynamic correction	-Bead height -Bead width	AWS ER70S-6 cooper coating
[28]	-Voltage -Speed rate	-Grain size -Microhardness	AWS ER70S-6
[29]	-Wire batches -Power modes -Wire feed speed -Travel speed	-Porosity size distribution	Aluminum alloy 2319
[30]	-Arc mode -Heat input -Interlayer wait-time -Scanning speed -Current -Voltage -Wire speed	-Maximum width -Effective width -Porosity -Grain maps -Ultimate tensile strength	AL-6Mg alloy

Table 3: Literature review for process parameters in other DED systems.

Type of energy source	Study	Process parameter	Outcome measures	Material
μ -plasma	[8]	-Current -Speed -Powder feeding rate	-Layer height -Layer width	H13 tool steel powder
	[31]	-Power -Travel speed -Wire feed rate	-Bead width -Bead height -Deposition quality	P20 tool steel wire
	[32]	-Power -Flow Rate of Powder -Travel Speed -Stand off distance -Plasma gas flow rate -Shield gas flow rate	-Bead width -Bead height -Quality of deposition	Ti6Al4V powder
Plasma wire deposition	[33]	-Wire feed speed -Travel speed Current	-Wall width -Effective wall width -Layer height	Ti6Al4V wire
Electron beam	[34]	-Power -Travel velocity -Wire feed rate	-Beta grain widths -Melt pool area	Ti6Al4V wire

a build space envelop of 365 mm x 170 mm x 300 mm through its X, Y, and Z axes, respectively. Standard g-code instructions developed using standard open source methods are used to generate the path trajectory of the positioning device.

The material, in powder form, is poured in the hopper. The powder flow rate is calibrated prior to deposition to ensure the rate in grams per minute is within the nominal range for the particular type of powder. The calibration is conducted at the start of every deposition run, and confirmed in triplicate. Whether the values diverge, the hopper can be screw in or out to adjust the flow of more or less powder, and repeat the calibration protocol. The powder density and morphol-

ogy are correlated to the powder flowability, as such, the powder flow rate calibration is critical.

The temperature of the plasma can reach more than 24,000 K [35]. Therefore, a cooling mechanism is necessary to prevent damages to the nozzle. A Koolant Kooler model JHI-1500-M is connected to the torch allowing $\sim 18\%$ propylene glycol in water to flow with a pressure of 551.58 kPa (80 psi). The thoriated tungsten electrode is sharpened to the angle of 20° and is set back 4 mm inside the torch nozzle. Two different torches were used in the experiments: the Excalibur PTA torch and the model 600 torch. The Excalibur torch was installed with a 3.18 mm ($1/8''$) nozzle suitable for small to medium applications. The plasma plume is slightly

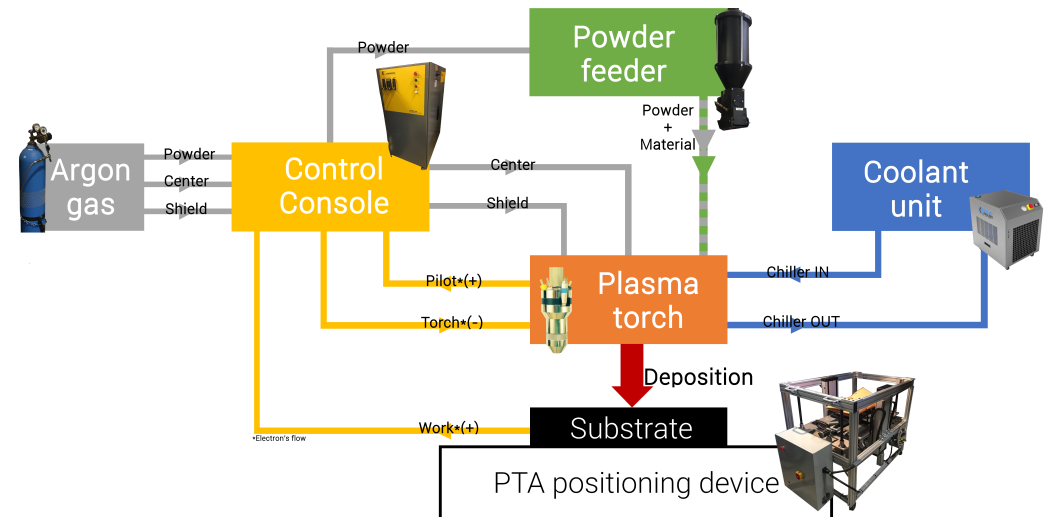


Fig. 2: PTA-AM System.

smaller than 4.76 mm (3/16”), which provides better bead control. The 600 torch was installed with a 2.38 mm (3/32”) long nose nozzle for low power applications. Table 4 provides the technical specification for each torch.

Although different torches and nozzles were used, the location of the powder exit port in the nozzle with respect to the deposition direction must be considered. Figure 3 shows the three cases considered for the experiments: 0, 45, and 90 degrees.

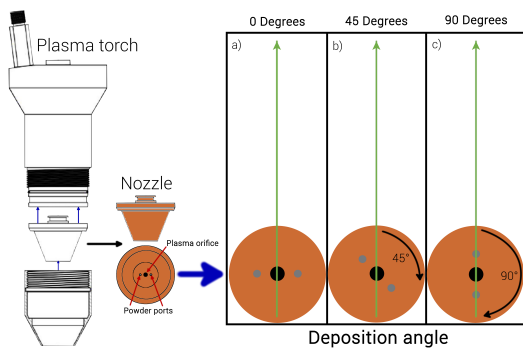


Fig. 3: Nozzle’s angle in relationship with the deposition direction a) 0 degrees, b) 45 degrees, and c) 90 degrees. The arrows indicate the travel direction.

The PTA positioning device lies under the fixed torch. An initial position for the building plate is set in the G-code to allow its movement into the single-track multiple-layers deposition. Figure 4 shows the path planning strategy to minimize the deposition collapse at the

ends of the layers [36, 37]. The length in the path planning corresponds to 130 mm, while the height for 27 layers. The transition distance between layers in the Z and X directions at the ends of each track is 0.75 mm and 3.5% of the length, respectively.

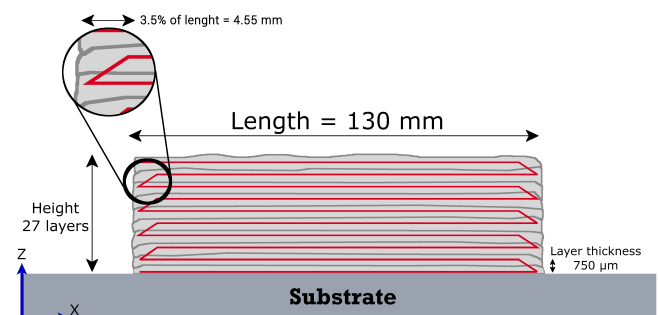


Fig. 4: Single-track multiple-layer deposition strategy.

The powder is a pre-blended mixture of tungsten carbide and a nickel alloy sourced from CErlikon Metco [38] and the trade name is PlasmaDur 51122. This powder contains monocrystalline Tungsten Carbide with Nickel-Chromium Boron Silicon powder. The morphology of the carbide is angular, while the matrix is spheroidal. Nominal particle size distribution is +63 to -180 μm, with a nominal apparent density of 5-6.5 g/cm³. Table 5 presents the chemical composition ranges of the hard phase and the matrix alloy.

The substrates are 152.40 mm x 152.40 mm x 6.35 mm (6” x 6” x 1/4”) hot-rolled flat bars made of ASTM A36 steel [Table 6]. The plate is washed with an indus-

Table 4: Operational ranges for the Excalibur and 600 torches.

Nozzle description	Weld current	Powder flow rate	Center gas flow	Electrode	Shield gas flow
	Amperes	grams/min	SLPM	Size (dia.)	SLPM
Excalibur torch standard 3.18 mm (1/8") 2 port	20 - 180	20 - 70	1 - 2	3.18-4.76 mm 1/8" - 3/16"	10 - 15
600 torch long nose 2.38 mm (3/32") 2 port	20 - 80	10 - 40	0.8 - 2	3.18 mm 1/8"	10 - 15

Table 5: Chemical composition ranges of the metal matrix composite [38].

Product	Hard Phase Composition (wt. %)			Matrix Alloy Composition (wt. %)						
	Phase %	W	C	Phase %	Ni	Cr	B	Si	C	Fe
PlasmaDur 51122	60	93.8 94.0	6.0 6.2	40	Bal.	9.5 12.5	2.0 2.5	3.3 4.3	0.3 0.6	2.0 3.5

Table 6: Chemical composition of the substrate [40].

wt%	C	Cu	P	Si	S	Fe
ASTM A36 steel	0.26	0.2	0.04	0.4	0.05	Bal.

trial cleaner to remove residual oils before getting sand-blasted. An Empire Pro-Finish® cabinet with a #36 mesh brown aluminum oxide grit at a pressure of 551.58-620.53 KPa (80-90 psi) is used to obtain a near-white metal surface finish in the substrates [39].

Table 7 lists the PTA-AM process parameters, the corresponding capability ranges, and the level values evaluated in this preliminary experimentation method.

A Taguchi-based DOE model method was used to preliminary analyze the effect of the process parameters on the build geometry and internal quality. The assessment includes eight process parameters considering seven factors with three levels, and one factor with two levels. An L18 orthogonal array identify the significant factors (Table 8). The experiment consisted of depositing 18 multi-layer single track samples with orthogonal combinations of the process parameter levels. As stated in the deposition strategy, each sample aims to measure 130 mm in length, and 27 layers in height. To be considered a successful experiment, the bead sample has to successfully complete the G-code through all the layers; otherwise, it is a failure. To characterize the as-built parts, a Struers Discotom-65 diamond saw sliced each sample into four cross-sections. As an outcome measurement, the weight of a one 20 mm section is employed. The remaining three sections were ground

and polished up to 0.05 microns to observe any internal porosity and metallurgical defects.

The Taguchi method provides information about the contribution of process parameters to specific outcomes. Consequently, the outcome have a specific goal which is quantifiable through the signal-to-noise ratio (SNR) measurements. The resultant values measure the variability to a nominal or target value under different conditions depending on the goals of the experiment. The outcome measures and the goals expected from the 18 runs are:

- Bead height: The height through the bead is measured for the cross-sections. The goal is to maximize the deposition; hence, the height. Equation (1) describes the larger-the-better signal-to-noise ratio [41] goal:

$$\eta = -10 \text{Log}_{10} \left(\frac{1}{n} \sum_{i=1}^n \frac{1}{Y_i^2} \right) \quad (1)$$

where n is the number of observations in each experiment, and Y_i is the observed measurement.

- Bead width: The outcome measurement is multiple measurements of the bead width on each of the runs for the different cross-sections. The goal is to obtain a nominal value, and the variance around this value can be considered the result of the noise factors. This goal searches for standardized width through the deposition, consequently, the importance of numerous measurements. The nominal-the-best signal-

Table 7: Process parameters, ranges, and DOE levels.

Process parameter	Value range	DOE value
Torch type	<i>Excalibur or 600 torch</i>	(P1) L1: Excalibur L2: 600 torch
Powder gas	<i>1-4 slpm</i>	(P2) L1: 1.5 L2: 2 L3: 2.5
Shield gas	<i>10-15 slpm</i>	(P3) L1: 10 L2: 12.5 L3: 15
Center gas	<i>1-2 slpm</i>	(P4) L1: 1 L2: 1.5 L3: 2
Nozzle's angle	<i>0°-90°</i>	(P5) L1: 0° L2: 45° L3: 90°
Powder flow rate	<i>20-40 grams/min</i>	(P6) L1: 20 L2: 30 L3: 40
Current	<i>20-80 A</i>	(P7) L1: 40 L2: 50 L3: 60
Travel Speed	<i>50-4,000 mm/min</i>	(P8) L1: 500 L2: 600 L3: 700
Stand-off distance	<i>2.5-13 mm</i>	<i>FIXED: 7 mm</i>

Table 8: L18 Taguchi orthogonal array combinations.

Runs	Process parameters levels							
	P1	P2	P3	P4	P5	P6	P7	P8
1	1	1	1	1	1	1	1	1
2	1	1	2	2	2	2	2	2
3	1	1	3	3	3	3	3	3
4	1	2	1	1	2	2	3	3
5	1	2	2	2	3	3	1	1
6	1	2	3	3	1	1	2	2
7	1	3	1	2	1	3	2	3
8	1	3	2	3	2	1	3	1
9	1	3	3	1	3	2	1	2
10	2	1	1	3	3	2	2	1
11	2	1	2	1	1	3	3	2
12	2	1	3	2	2	1	1	3
13	2	2	1	2	3	1	3	2
14	2	2	2	3	1	2	1	3
15	2	2	3	1	2	3	2	1
16	2	3	1	3	2	3	1	2
17	2	3	2	1	3	1	2	3
18	2	3	3	2	1	2	3	1

to-noise ratio [41] is described as:

$$\eta = 10 \text{Log}_{10} \left(\frac{\mu^2}{\sigma^2} \right) \quad (2)$$

where η is the signal-to-noise ratio, μ is the mean of the measurements, and σ^2 is the variance.

- **Bead Weight:** Similarly to bead height, the goal for the weight outcome measurement is to build up a more substantial deposition. Therefore, a larger-the-better signal-to-noise ratio strategy is required. The difference with the bead height outcome is the amount of data collected since only one 20 mm in length cross-section is weighted for each experiment.

- **Porosity:** In contrast, to ensure that we are maximizing the mechanical properties for the heavy-duty industry (i.e. wear and corrosion resistance), the internal porosity needs to be reduced. Accordingly, the outcome measurement is the porosity percentage of the cross-sections. The internal porosity was calculated using the software ImageJ. Image processing techniques are required to differentiate between pores and WC particles. As a signal-to-noise ratio [41], a strategy of smaller-the-best is depicted in equation (3):

$$\eta = -10 \text{Log}_{10} \left(\frac{1}{n} \sum_{i=1}^k Y_i^2 \right) \quad (3)$$

3 Results and discussion

Due to the lack of understanding of the process and its complexity, only five experiments achieved successful printing conditions in these preliminary experiments. Failures were classified in the following categories:

- A) No deposition:** In this category, the runs 6 and 17 have a powder quantity of 20 grams per minute. The amount of feedstock material is not enough to generate mass for the formation of a melt pool. In the runs 9, 14, and 16, the current input is 40 A. The amount of heat input in these runs is not enough to melt the MMC and create a deposition.
- B) Intermittent deposition:** In the elements from the previous category, the powder and heat input influences avoid a deposition. However, if the travel

speed is reduced, more energy is input per volume unit. Run 1 has a low powder quantity and current, but it has as well low travel speed. The low speed allows the generation of a melt pool, but it is not enough to generate coalescence for a continuous deposition, and the deposition is intermittent. This phenomenon is better known as the balling effect. For the runs 12 and 13, the powder quantity is low (20 grams per minute), but the nozzle generates a more concentrated plasma than the Excalibur torch due to the center bore reduction. The increase in heat input allows the melt pool generation but not enough for a continuous deposition.

- C) Collapse due to heat accumulation:** In the runs 3, 4, and 18, the heat input is the highest (60 A). This amount of energy input generates a heat accumulation in the deposition. As the printing continues, the thermal build-up keeps increasing to the point that the melt pool spreads, producing a bead's slumping, hindering the increment in layer thickness and increasing the bead width.
- D) Over-deposition:** The layer thickness for all the experiments is $750\ \mu\text{m}$ to keep a constant increase in the Z-axis. If the deposition of metal powder increases, on each layer, the stand-off-distance will decrease. For run 5, the nozzle angle at 90 degrees and the low travel speed (500 mm/min) produces an increment in the deposition. For run 8, the low speed produces a raise in the deposition.

The lack of deposition, such as in failures A to C, increases the stand-off-distance, increasing the process voltage. The distance increment induces a rise in the voltage, which generates unstable plasma operation for the PTA. Over-deposition, on the other hand, can create a short-circuit due to the low stand-of-distance between the torch and the deposit. Table 9 shows a summary of the experimental results.

Figure 5 shows the cross-section results for the successful experiments number 2, 7, 10, 11 and 15. These images provide the information to measure the bead height, width, and porosity. Each image was calibrated with the corresponding scale bar and taken from the left, middle, and right sections.

In the case of run 2 (Fig. 5a), although the width of the bead is steady, the middle section has higher deposition than the ends of the bead. This observation is consistent with the macro-scale information of the collapsing at the end of the track as shown previously in Table 9. This effect is common in single-track multiple-

layers beads due to the deposition collapse at the ends. The deposition at the ends of the beads is continuous; therefore, thermal strain increases at the ends, causing this type of distortion as reported in Mukherjee et al. [42]. Additionally, porosity is higher in the right section, and some WC particles are settling on top of the left section. These are indicators of higher settling rates of the carbide which has a significantly higher density than the metal matrix. This carbide free region at the top can be minimized with higher solidification rates and/or lower overall heat input. For run 7 (Fig. 5b), the bead is homogeneous among the sections, and less porosity is observed compared to run 2. Although the results are good at this scale, on the macro-scale, one side is collapsed in right section, and a notable increment in height through the bead is detected. The one-sided phenomenon can be linked to the perturbations of the start of the plasma arc. Higher powder flow gas can generate turbulent flows hindering the deposition in the transition to a steady-state. In the case of run 10 (Fig. 5c), the bead's width shows significant differences in the cross-sections. Higher porosity is present at the ends, while WC settling is in the left and middle sections. It is essential to highlight that from all the samples, this bead was not attached to the substrate, indicating poor bonding between the bead and the substrate. As the heat flow from the bead out to the substrate, deposition was hindered due to lack of bonding, and the left section shows a slumping effect due to heat accumulation. At taller builds, stable heat distribution plays an important role in maintaining geometric consistency [43, 44]. Figure 5d illustrates the results of run 11. Through the sections, carbide settling is observed. This phenomenon is an indicator of the slow solidification of the Nickel matrix due to heat accumulation. Another consequence of thermal build-up is the geometry deformation. The sample exhibits a broader and shorter shape compared to other samples. A low dilution with the substrate is the rationale for this anomaly. Run 15 is depicted in Figure 5e. Considerable carbide settling is identified at the top of the middle section. Left and right sections display slumping events with moderate WC settle.

Figure 6 shows the descriptive statistics for the bead width in the successful experiments. Run 2 exhibits better width stability based on its standard deviation, while run 15 is the more unstable. Run 15 has higher powder and shield gas than run 2, which can influence the stability of the deposition. Moreover, the speed in run 15 is slower, yielding to higher heat concentration notable on the green oxide attached to the bead.

Table 9: L18 Taguchi orthogonal array combinations results.

Run	Result	Comment
1	Failure type B	Intermittent deposition due to balling effect
2		Collapsing at ends of track
3	Failure type C	Collapse due to heat accumulation
4	Failure type C	Collapse due to heat accumulation
5	Failure type D	Over-deposition
6	Failure type A	No deposition
7		One side collapse and uneven height
8	Failure type D	Over-deposition
9	Failure type A	No deposition
10		Uneven height and width
11		Shorter and fewer deposition
12	Failure type B	Intermittent deposition due to balling effect
13	Failure type B	Intermittent deposition due to balling effect
14	Failure type A	No deposition
15		Unstable deposition and uneven width
16	Failure type A	No deposition
17	Failure type A	No deposition
18	Failure type C	Collapse due to heat accumulation

For the Taguchi DOE preliminary analysis, the software Statistica was implemented. Table 10 shows the SNR results for the measured outcomes considering their respective goals. Signal-to-noise ratios provide a vision of each run's performance towards the outcomes; higher SNR means better performance. Information from failed samples in the height and weight analysis were manually measured and considered. For the case of width and porosity, the data could not be measured, and their signal-to-noise ratios were calculated as zero.

Figure 7 shows the mean plot results for the outcome variables. These graphs represent how susceptible are the responses to the process parameters. Figure 7a demonstrates that the powder flow rate (by 34%), powder gas (by 21%), and travel speed (by 17%) have a more significant impact on the bead height. The results prompt that in order to increase the bead height, more material is needed. Additionally, higher deposition rates can be obtained by decreasing the travel speed. Width standardization is principally affected by current (by 36%), powder flow rate (by 19%), and powder gas (by

Table 10: Signal-to-Noise ratio results in dBi.

Run	Height	Width	Weight	Porosity
1	19.20	0.00	14.30	0.00
2*	24.89	37.15	22.79	-2.57
3	21.93	0.00	16.36	0.00
4	15.94	0.00	5.98	0.00
5	23.73	0.00	15.80	0.00
6	15.08	0.00	10.03	0.00
7*	24.65	30.96	22.75	6.48
8	16.31	0.00	9.03	0.00
9	10.98	0.00	-4.07	0.00
10*	24.47	19.22	22.72	-1.26
11*	21.51	27.61	22.46	5.84
12	14.73	0.00	11.39	0.00
13	13.20	0.00	10.69	0.00
14	10.17	0.00	-0.70	0.00
15*	22.92	13.92	19.81	5.58
16	16.19	0.00	15.46	0.00
17	4.24	0.00	-5.55	0.00
18	17.97	0.00	11.84	0.00

The star (*) elements represent the successful runs.

17%) (Fig. 7b). An even heat distribution during the deposition process is essential to standardized width. A

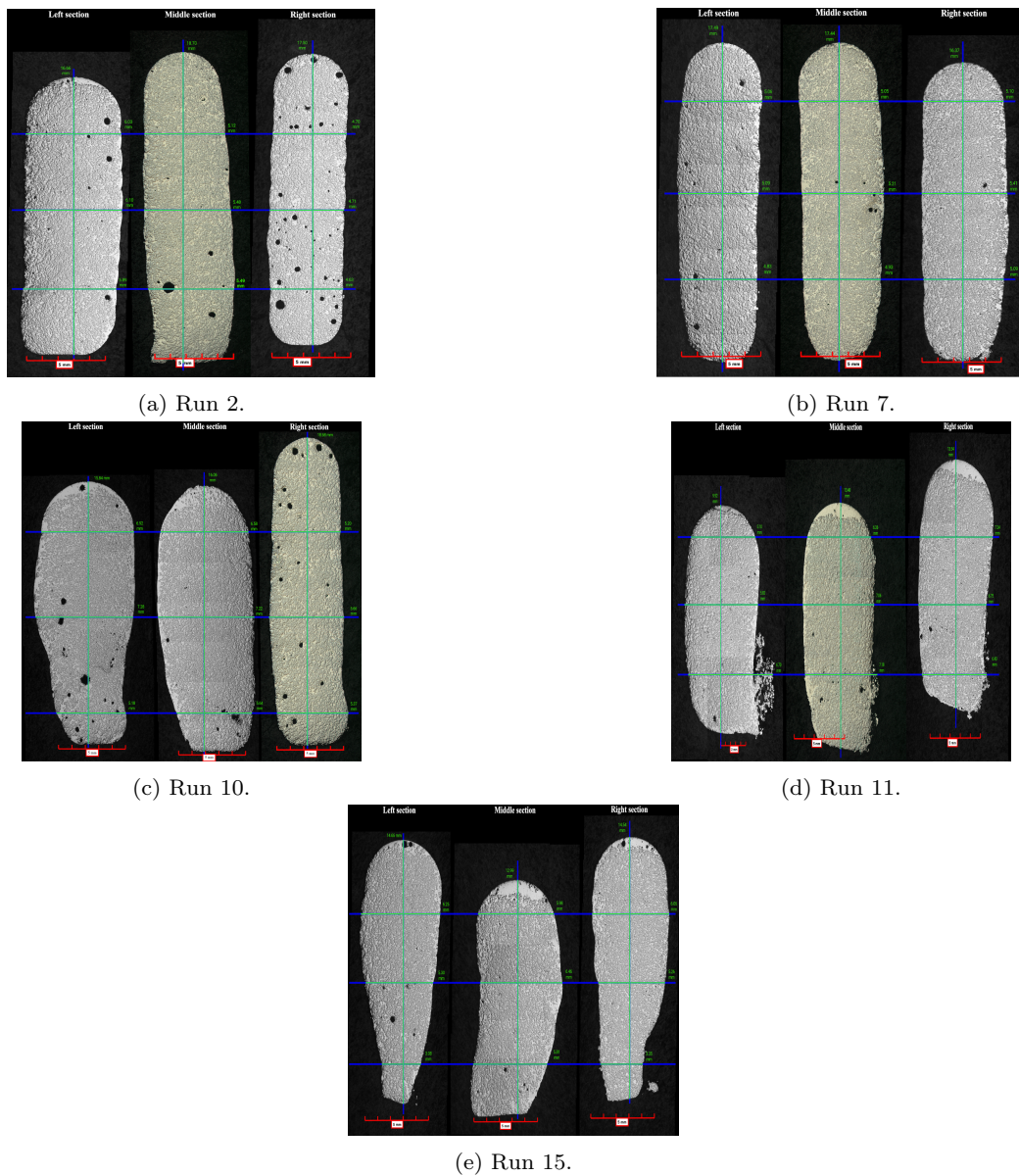


Fig. 5: Single-track multiple-layers cross-sections results taken from left to right relative to the front view of the bead.

high current produces heat accumulation and deformations; low current generates low dilution and unstable deposition. In the results of the weight, it is interesting to identify that similar process parameters to bead height are influencing the outcome: powder flow rate (by 29%), powder gas (by 25%), and travel speed (by 12%). Moreover, other parameters such as center gas (by 11%) and current (by 10%) became more meaningful (Fig. 7c). Similarly, increment in weight is closely related to higher deposition shown by the comparison between the height and weight mean plots. Regarding the porosity, the powder flow rate is the parameter with the most substantial effect by 52%, followed by the nozzle

angle (by 19%) and the center gas (by 16%) (Fig. 7d). Results indicate that higher deposition rates lead to lesser voids in the bead. Interestingly, a zero degree angle generates a symmetrical deposition reducing the probability of process-induced porosity [45]. By reducing the center gas, less gas can become entrapped within the melt pool, and the porosity is decreased [46].

The information obtained from the mean plots provides a combination of process parameters for a better performance of the desired output. Table 11 shows a preliminary process parameter's combinations proposal and the analytically calculated signal-to-noise ratio

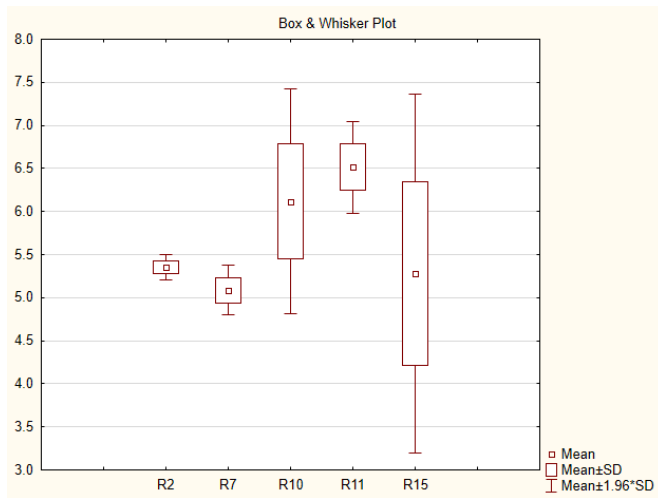
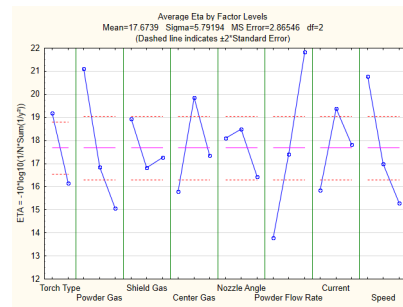


Fig. 6: Descriptive statistics for the bead width.

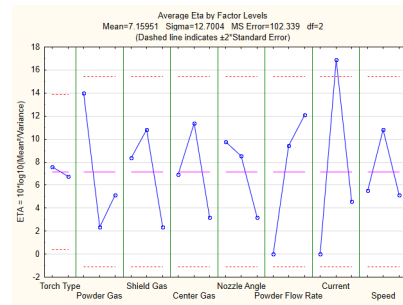
tio. The last row yields to an overall recommendation considering the frequency of the levels over the outcomes. Notably, for the nozzle angle, the frequencies of the levels are matched; therefore, the criteria of higher deposition is selected. The recommended process parameters obtained in this preliminary work are a stand-off-distance of 7 mm using the Excalibur torch, a powder gas flow of 1.5 SLPM, a shielding gas flow of 10 SLPM, a center gas flow of 1.5 SLPM, a nozzle’s angle of 45 degrees, a powder flow rate of 40 grams/min, a current of 50 A, and a travel speed of 500 mm/min.

Additional analysis of the samples in the microstructural domain were completed. Figure 8 shows the micrograph results for run 15 at two different magnifications. A uniform distribution of tungsten carbide particles in the nickel matrix was observed without a significant degradation of the tungsten carbide particles. The results exhibit that changes in the process parameters do not affect significantly carbides in the envelope of ranges that the experiments were executed.

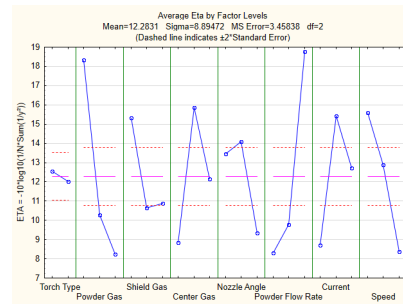
EDS elemental maps of the as-built composite are illustrated in (Fig. 9a). In addition to W-enriched particles (tungsten carbides), some small Cr-enriched particles can be observed. To determine the phase of these particles, X-Ray diffraction (XRD) analysis was conducted. From XRD pattern of the composite (Fig. 9b), the Cr-enriched particles were found to be $Cr_{23}C_6$. Moreover, Ni_3Si and Ni_3B phases were detected by XRD, whose formation was attributed to the presence of Si and B in the nickel alloy matrix. The micrographs and EDX results are expected for this type of material.



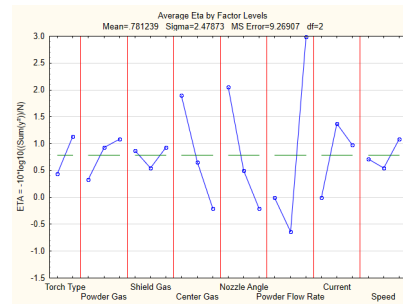
(a) Height.



(b) Width.



(c) Weight.



(d) Porosity.

Fig. 7: Mean plot results for the Taguchi design of experiments.

4 Validation

Three samples were printed with the obtained process parameters combinations of Table 11. Figure 10 shows the front, sides, and top views of the samples for height

Table 11: Process parameters combinations to improve the outcomes and its recommended overall proposal.

Outcome measure	P1	P2	P3	P4	P5	P6	P7	P8	Expected SNR dBi
Height	1	1	1	2	2	3	2	1	35.86
Weight	1	1	1	2	2	3	2	1	39.96
Width	1	1	2	2	1	3	2	2	43.11
Porosity	2	3	3	1	1	3	2	3	7.06
Overall	1	1	1	2	2	3	2	1	

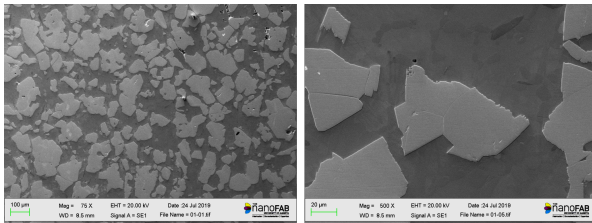
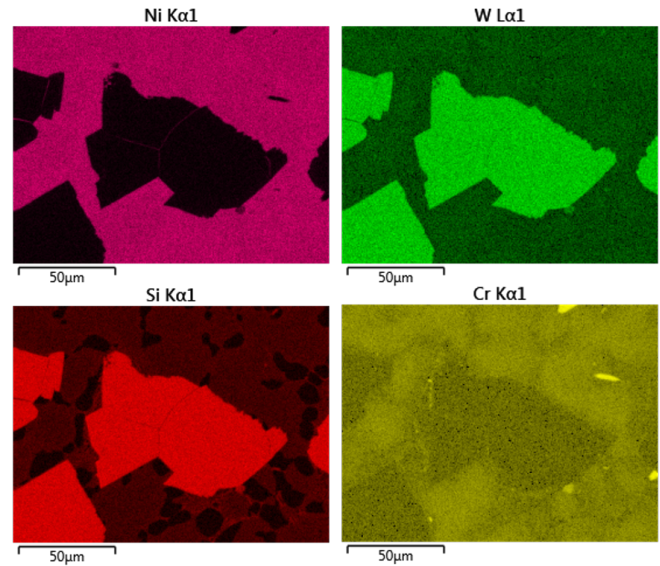


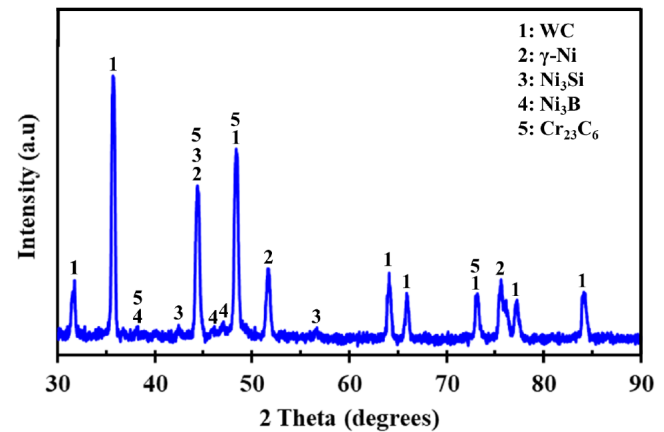
Fig. 8: Micrograph analysis of run 15.

and weight called Proposal A (Fig. 10a), for width called Proposal B (Fig. 10b), and for porosity called Proposal C (Fig. 10c). Qualitative observations disclose improvement results for the height and width outcomes. Proposal A is the higher bead with some perturbation on top due to the deposition effect of the nozzle angle. The side views show some instability during the building of the layers. Bead Proposal B definitely shows a steady bead width through the layers. In the case of the porosity results, the increment in the travel speed caused a lack of continuous coalescence in the bead producing columnar depositions. This phenomenon was not presented in any of the 18 runs. Runs 1, 12, and 13 produced a balling effect, although the travel speed was 500, 700, and 600 mm/min, respectively. The powder flow rate used in these runs was too low to allow the columnar deposition (20 grams/min). The columnar deposition was not expected, and for that reason, the measurement and comparison of the porosity sample could not be obtained.

With the aid of a Sick laser profilometer, twelve points were selected to measure bead height and width quantitatively. For the height and weight Proposal A bead, the average height was 24.20 mm with a standard deviation of 0.34 mm, and the average width was 6.23 with a standard deviation of 0.33 mm. Regarding Proposal B bead, the height averaged 22.87 mm with a standard deviation of 0.21 mm and the width 5.40 mm with 0.13 mm of standard deviation. In the case of the porosity Proposal C bead, average height was 19.18 mm with a standard deviation of 8.86 mm, and width averaged 5.39 mm with 1.13 mm of standard deviation. A 20 mm section was sliced for each bead and weighted.



(a) Chemical analysis.



(b) X-Ray diffraction analysis.

Fig. 9: Micro-scale analyses.

The values obtained were 18.67 g, 17.71 g, and 8.62 g for Proposals A, B, and C, respectively. Figure 11 exhibits the descriptive statistics for height and width through samples A to C.

Quantitative information confirms that the Proposal A improves the height and weight outcomes. The height difference between Proposal A and B is of 5.82%, which

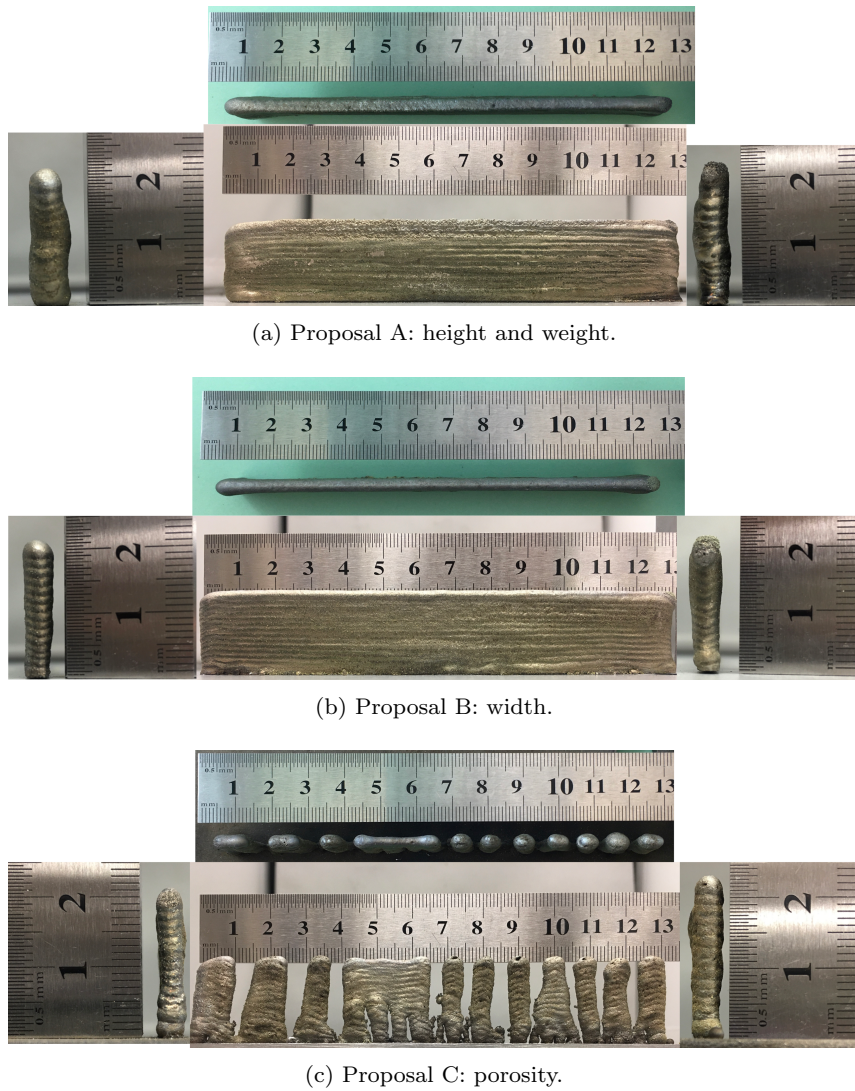


Fig. 10: Proposal printings for outcome improvement.

could be only because of the additional perturbations that sample A exhibits due to the nozzle orientation. Similarly, the weight difference is of 5.42%, and it is due to the additional deposition in sample A. On the other hand, Proposal A has 26.17% and 116.58% more height and weight compared to Proposal C. Comparing it to the best result in the experiments, the Proposal A improves by 29.41% the height and by 35.39% the weight.

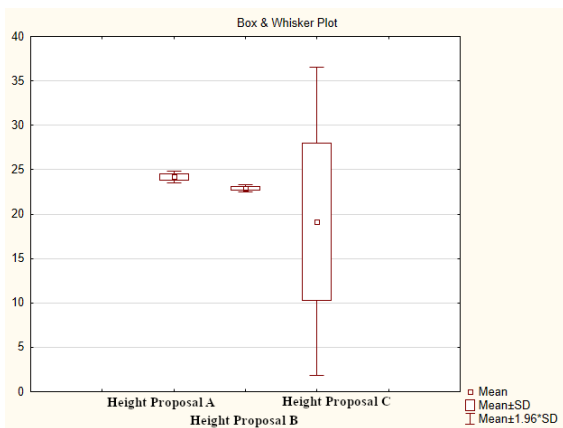
Regarding bead width, the standard deviation in Proposal A is 153.85% more than the standard deviation of Proposal B. Additionally, the standard deviation of Proposal C is 769.23% more than the standard deviation of Proposal B. That confirms that sample B has less variance and standardized width through the deposition. Comparing it to the preliminary experiments'

most regular width (Run 2), the standard deviation decreased by 46.15%. This difference is due to the differences in the measurement resolution, although the deposition in Proposal B is more balance than Run 2.

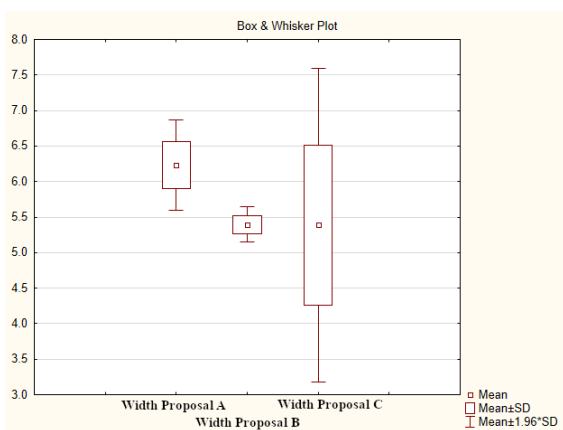
From the data collected in the Proposals, the SNR for the height, width, and weight can be calculated as 27.67 dBi, 40.09 dBi, and 25.42 dBi, respectively. It is demonstrated that the method worked for improving the height SNR by 11.19%, the width SNR by 7.9%, and the weight SNR by 11.55%.

5 Conclusion

This work provided a methodology through the Taguchi-based design of experiments for preliminary understanding the repercussion of process parameters in geometri-



(a) Optimal Height descriptive statistics.



(b) Optimal Width descriptive statistics.

Fig. 11: Descriptive statistics results for the height and width in the optimal beads.

cal and microstructural characteristics. The SNR in the outputs grant an overlook of the performance toward the goals. The results showed the importance of an appropriate bonding between the part and the substrate to allow stable thermal dissipation. Heat accumulation induces perturbations in the build-up process producing deformed structures such as those seen in Proposal C. This slumping effect hinders the deposition process and increases the solidification time. For metal composites with considerable different densities, a decrease in the cooling rates results in settling of the denser reinforcement particle, which can lead to poor performance in service.

Bead height and weight are mainly affected by the powder flow rate, the powder gas flow rate, and the travel speed. These outcomes are coupled, the higher the deposition, the more material is in there; hence, an increment in weight. There is no coupling with the width because the outcome goal is to minimize the vari-

ance, not maximizing the width. An arise in the deposition takes effect by increasing the material flow input and reducing the travel speed. Parameters such as current and powder flow rate, greatly influence the fluctuation of the bead width. As stated previously, a higher current generates overheating of the bead warping it. A low powder flow rate or low current inhibits the deposition process due to a lack of material or energy. Lowering these parameters generates a balling effect or no deposition. The plasma shape also affects the bead width with different stand-off-distances, but this work kept that parameter fixed. Concerning the porosity, the results depicted a direct correlation between high powder flow rate and low porosity, although given the outcome in the Proposal C, the results must be taken with prudence. The anomaly might be originated due to process-induced effects such as the turbulent flow under the torch. The phenomenon will later be analyzed by the use of high-speed cameras to add further information to this matter. One process parameter was consistent with being crucial to every outcome, the powder flow rate. The upper limitation on the 600 torch constraints the maximum amount of powder flow; hence, further experiments require increased flow rates by using the Excalibur torch, so the 600 torch is not suitable for the AM applications.

The PTA-AM process exhibits generally uniform carbide distribution though the deposition height. The results display a high quality of the composite after the printing process as seen with the low carbide degradation within the analyzed operational ranges. Therefore, this advanced manufacturing process is suitable for application in the heavy-duty industry where wear is a concern. The methodology validates the impact of process parameters into quantifiable outcomes to understand the deposition process and achieve near net-shaped components.

Acknowledgements This research was funded by the Natural Sciences and Engineering Research Council of Canada (NSERC) grant numbers RGPIN-2016-04689, CRDPJ 514752-17, Innotech Alberta under the intern project ATS-2017-IN-028, the Mexican National Council for Science and Technology (CONACYT) under the register 234809 and 440868, and Tecnológico de Monterrey under its program of professor in development.

Conflict of interest

The authors declare that they have no conflict of interest.

References

1. S. Kalpakjian and S.R. Schmid. *Manufacturing Engineering and Technology*. Pearson, 2001. ISBN 978-0-13-522860-9.
2. J.G. Mercado Rojas, T. Wolfe, B.A. Fleck, and Ahmed Jawad Qureshi. Plasma transferred arc additive manufacturing of Nickel metal matrix composites. *Manufacturing Letters*, 2018. ISSN 22138463. doi: 10.1016/j.mfglet.2018.10.001.
3. P. Wu, H. M. Du, X. L. Chen, Z. Q. Li, H. L. Bai, and E. Y. Jiang. Influence of WC particle behavior on the wear resistance properties of Ni-WC composite coatings. *Wear*, 257(1-2):142–147, 2004. ISSN 00431648. doi: 10.1016/j.wear.2003.10.019.
4. ASTM-F3187. Standard Guide for DED of Metals, 2016.
5. Adrita Dass and Atieh Moridi. State of the Art in Directed Energy Deposition: From Additive Manufacturing to Materials Design. *Coatings*, 9(7): 418, jun 2019. ISSN 2079-6412. doi: 10.3390/coatings9070418.
6. T. Artaza, A. Alberdi, M. Murua, J. Gorrotxategi, J. Frías, G. Puertas, M.A. Melchor, D. Mugica, and A. Suárez. Design and integration of WAAM technology and in situ monitoring system in a gantry machine. *Procedia Manufacturing*, 13:778–785, 2017. ISSN 23519789. doi: 10.1016/j.promfg.2017.09.184.
7. Scott M. Thompson, Linkan Bian, Nima Shamsaei, and Aref Yadollahi. An overview of Direct Laser Deposition for additive manufacturing; Part I: Transport phenomena, modeling and diagnostics. *Additive Manufacturing*, 8:36–62, 2015. ISSN 22148604. doi: 10.1016/j.addma.2015.07.001.
8. H Wang, W Jiang, M Valant, and R Kovacevic. Microplasma powder deposition as a new solid freeform fabrication process. *Proceedings of the Institution of Mechanical Engineers, Part B: Journal of Engineering Manufacture*, 217(12): 1641–1650, 12 2003. ISSN 0954-4054. doi: 10.1243/095440503772680578.
9. Douglas C. Montgomery. *Design and Analysis of Experiments*. Wiley, 2019. ISBN 978-1-119-49244-3.
10. Abhay Sharma, Navneet Arora, and Bhanu K. Mishra. A practical approach towards mathematical modeling of deposition rate during twin-wire submerged arc welding. *The International Journal of Advanced Manufacturing Technology*, 36(5-6):463–474, 3 2008. ISSN 0268-3768. doi: 10.1007/s00170-006-0847-1.
11. S. C. Juang and Y. S. Tarn. Process parameter selection for optimizing the weld pool geometry in the tungsten inert gas welding of stainless steel. *Journal of Materials Processing Technology*, 122(1): 33–37, 2002. ISSN 09240136. doi: 10.1016/S0924-0136(02)00021-3.
12. Mohammad K. Alam, Ruth Jill Urbanic, Navid Nazemi, and Afsaneh Edrissy. Predictive modeling and the effect of process parameters on the hardness and bead characteristics for laser-cladded stainless steel. *International Journal of Advanced Manufacturing Technology*, 94(1-4):397–413, 2018. ISSN 14333015. doi: 10.1007/s00170-017-0898-5.
13. Navid Nazemi, Jill Urbanic, and Mohammad Alam. Hardness and residual stress modeling of powder injection laser cladding of P420 coating on AISI 1018 substrate. *International Journal of Advanced Manufacturing Technology*, 93(9-12):3485–3503, 2017. ISSN 14333015. doi: 10.1007/s00170-017-0760-9.
14. Subrata Mondal, Asish Bandyopadhyay, and Pradip Kumar Pal. Application of artificial neural network for the prediction of laser cladding process characteristics at Taguchi-based optimized condition. *International Journal of Advanced Manufacturing Technology*, 70(9-12):2151–2158, 2014. ISSN 02683768. doi: 10.1007/s00170-013-5393-z.
15. Bhaskarananda Dasgupta and Pinaky Bhadury. Optimization of Weld Bead Parameters of Nickel Based Overlay Deposited by Plasma Transferred Arc Surfacing with Adequacy Test. *International Journal of Engineering Research and Applications*, 4(7):201–206, 2014.
16. J. Wilden, J. P. Bergmann, and H. Frank. Plasma transferred arc welding—modeling and experimental optimization. *Journal of Thermal Spray Technology*, 15(4):779–784, 2006. ISSN 1059-9630, 1544-1016. doi: 10.1361/105996306X146767.
17. R. Parekh, R.K. Buddu, and R.I. Patel. Multi-physics Simulation of Laser Cladding Process to Study the Effect of Process Parameters on Clad Geometry. *Procedia Technology*, 23:529–536, 2016. ISSN 22120173. doi: 10.1016/j.protcy.2016.03.059.
18. S. M. Saqib and R. J. Urbanic. Investigation of the Transient Characteristics for Laser Cladding Beads Using 420 Stainless Steel Powder. *Journal of Manufacturing Science and Engineering*, 139(8):081009, 2017. ISSN 1087-1357. doi: 10.1115/1.4036488.
19. Chigozie Obidigbo, Eric-Paul Tatman, and Joy Gockel. Processing parameter and transient effects on melt pool geometry in additive manufacturing of Invar 36. *The International Journal of Advanced Manufacturing Technology*, 104 (5-8):3139–3146, oct 2019. ISSN 0268-3768. doi:

- 10.1007/s00170-019-04229-5.
20. J. Beuth and N. Klingbeil. The role of process variables in laser-based direct metal solid freeform fabrication. *Jom*, 53(9):36–39, 2001. ISSN 10474838. doi: 10.1007/s11837-001-0067-y.
 21. Alireza Fathi, Ehsan Toyserkani, Amir Khajepour, and Mohammad Durali. Prediction of melt pool depth and dilution in laser powder deposition. *Journal of Physics D: Applied Physics*, 39(12):2613–2623, 6 2006. ISSN 0022-3727. doi: 10.1088/0022-3727/39/12/022.
 22. Huan Qi, Magdi Azer, and Prabhjot Singh. Adaptive toolpath deposition method for laser net shape manufacturing and repair of turbine compressor airfoils. *International Journal of Advanced Manufacturing Technology*, 48(1-4):121–131, 2010. ISSN 02683768. doi: 10.1007/s00170-009-2265-7.
 23. Andrea Angelastro, Sabina L. Campanelli, Giuseppe Casalino, and Antonio D. Ludovico. Optimization of Ni-based WC/Co/Cr composite coatings produced by multilayer laser cladding. *Advances in Materials Science and Engineering*, 2013, 2013. ISSN 16878434. doi: 10.1155/2013/615464.
 24. Tarak Amine, Joseph W. Newkirk, and Frank Liou. An investigation of the effect of direct metal deposition parameters on the characteristics of the deposited layers. *Case Studies in Thermal Engineering*, 3(9-12):21–34, 7 2014. ISSN 2214157X. doi: 10.1016/j.csite.2014.02.002.
 25. S. Saqib, R.J. Urbanic, and K. Aggarwal. Analysis of Laser Cladding Bead Morphology for Developing Additive Manufacturing Travel Paths. *Procedia CIRP*, 17:824–829, 2014. ISSN 22128271. doi: 10.1016/j.procir.2014.01.098.
 26. Ali Gökhan Demir. Micro laser metal wire deposition for additive manufacturing of thin-walled structures. *Optics and Lasers in Engineering*, 100(January 2018):9–17, 2018. doi: 10.1016/j.optlaseng.2017.07.003.
 27. J.L. Prado-Cerqueira, J.L. Diéguez, and A.M. Camacho. Preliminary development of a Wire and Arc Additive Manufacturing system (WAAM). *Procedia Manufacturing*, 13:895–902, 2017. ISSN 23519789. doi: 10.1016/j.promfg.2017.09.154.
 28. Mariacira Liberini, Antonello Astarita, Gianni Campatelli, Antonio Scippa, Filippo Montevecchi, Giuseppe Venturini, Massimo Durante, Luca Boccarusso, Fabrizio Memola Capece Minutolo, and A. Squillace. Selection of Optimal Process Parameters for Wire Arc Additive Manufacturing. *Procedia CIRP*, 62:470–474, 2017. ISSN 22128271. doi: 10.1016/j.procir.2016.06.124.
 29. E. M. Ryan, T. J. Sabin, J. F. Watts, and M. J. Whiting. The influence of build parameters and wire batch on porosity of wire and arc additive manufactured aluminium alloy 2319. *Journal of Materials Processing Technology*, 262(April):577–584, 2018. ISSN 09240136. doi: 10.1016/j.jmatprotec.2018.07.030.
 30. Chen Zhang, Yufei Li, Ming Gao, and Xiaoyan Zeng. Wire arc additive manufacturing of Al-6Mg alloy using variable polarity cold metal transfer arc as power source. *Materials Science and Engineering A*, 711(August 2017):415–423, 2018. ISSN 09215093. doi: 10.1016/j.msea.2017.11.084.
 31. Suyog Jhavar, N. K. Jain, and C. P. Paul. Development of micro-plasma transferred arc (μ -PTA) wire deposition process for additive layer manufacturing applications. *Journal of Materials Processing Technology*, 214(5):1102–1110, 2014. ISSN 09240136. doi: 10.1016/j.jmatprotec.2013.12.016.
 32. Mayur S. Sawant and N. K. Jain. Investigations on additive manufacturing of Ti-6Al-4V by microplasma transferred arc powder deposition process. *Journal of Manufacturing Science and Engineering, Transactions of the ASME*, 140(8):1–11, 2018. ISSN 15288935. doi: 10.1115/1.4040324.
 33. F. Martina, J. Mehnen, S. W. Williams, P. Colegrove, and F. Wang. Investigation of the benefits of plasma deposition for the additive layer manufacture of Ti-6Al-4V. *Journal of Materials Processing Technology*, 212(6):1377–1386, 2012. ISSN 09240136. doi: 10.1016/j.jmatprotec.2012.02.002.
 34. Joy Gockel, Jack Beuth, and Karen Taminger. Integrated control of solidification microstructure and melt pool dimensions in electron beam wire feed additive manufacturing of Ti-6Al-4V. *Additive Manufacturing*, 1-4:119–126, 10 2014. ISSN 22148604. doi: 10.1016/j.addma.2014.09.004.
 35. Wurikaixi Aiyiti, Wanhua Zhao, Bingheng Lu, and Yiping Tang. Investigation of the overlapping parameters of MPAW-based rapid prototyping. *Rapid Prototyping Journal*, 12(3):165–172, 2006. ISSN 13552546. doi: 10.1108/13552540610670744.
 36. Jun Xiong, Ziqiu Yin, and Weihua Zhang. Forming appearance control of arc striking and extinguishing area in multi-layer single-pass GMAW-based additive manufacturing. *International Journal of Advanced Manufacturing Technology*, 87(1-4):579–586, 2016. ISSN 14333015. doi: 10.1007/s00170-016-8543-2.
 37. Giuseppe Venturini, Filippo Montevecchi, Francesco Bandini, Antonio Scippa, and Gianni Campatelli. Feature based three axes computer aided manufacturing software for wire

- arc additive manufacturing dedicated to thin walled components. *Additive Manufacturing*, 22 (May):643–657, aug 2018. ISSN 22148604. doi: 10.1016/j.addma.2018.06.013.
38. Oerlikon Metco. Material Product Data Sheet Monocrystalline Tungsten Carbide / Nickel Chromium Boron Silicon Powder for Plasma Transferred Arc (PTA). Technical report, Oerlikon Metco, 2019.
 39. NACE. Joint Surface Preparation Standard Near-White Metal Blast Cleaning. Technical Report 21066, NACE International, 2006.
 40. ASTM. A36-A36M19 Standard Specification for Carbon Structural Steel. Technical report, ASTM, 2005.
 41. Prakash R. Apte. Why/When is Taguchi Method Appropriate? Chapter 5: Taguchi Method SN-Ratio for Quality Characteristics approaching IDEAL value, 2001.
 42. T. Mukherjee, V. Manvatkar, A. De, and T. DebRoy. Mitigation of thermal distortion during additive manufacturing. *Scripta Materialia*, 127:79–83, jan 2017. ISSN 13596462. doi: 10.1016/j.scriptamat.2016.09.001.
 43. C.R. Cunningham, J.M. Flynn, A. Shokrani, V. Dhokia, and S.T. Newman. Invited review article: Strategies and processes for high quality wire arc additive manufacturing. *Additive Manufacturing*, 22(June):672–686, 8 2018. ISSN 22148604. doi: 10.1016/j.addma.2018.06.020.
 44. Binta Wu, Donghong Ding, Zengxi Pan, Dominic Cuiuri, Huijun Li, Jian Han, and Zhenyu Fei. Effects of heat accumulation on the arc characteristics and metal transfer behavior in Wire Arc Additive Manufacturing of Ti6Al4V. *Journal of Materials Processing Technology*, 250(December 2016):304–312, 12 2017. ISSN 09240136. doi: 10.1016/j.jmatprotec.2017.07.037.
 45. W. J. Sames, F. A. List, S. Pannala, R. R. Dehoff, and S. S. Babu. The metallurgy and processing science of metal additive manufacturing. *International Materials Reviews*, 61(5):315–360, jul 2016. ISSN 0950-6608. doi: 10.1080/09506608.2015.1116649.
 46. Sarah K. Everton, Matthias Hirsch, Petros I. Stavroulakis, Richard K. Leach, and Adam T. Clare. Review of in-situ process monitoring and in-situ metrology for metal additive manufacturing. *Materials and Design*, 95:431–445, 2016. ISSN 18734197. doi: 10.1016/j.matdes.2016.01.099.